Journal of Solid State Chemistry 182 (2009) 442–450

Contents lists available at ScienceDirect

Journal of Solid State Chemistry

journal homepage: www.elsevier.com/locate/jssc

Lanthanum pyrochlores and the effect of yttrium addition in the systems $La_{2-x}Y_xZr_2O_7$ and $La_{2-x}Y_xHf_2O_7$

Karl R. Whittle [a,b,*], Lachlan M.D. Cranswick [c], Simon A.T. Redfern [b], Ian P. Swainson [c], Gregory R. Lumpkin [a,b]

[a] Institute of Materials Engineering, Australian Nuclear Science and Technology Organisation, PMB 1, Menai, NSW 2234, Australia
[b] Department of Earth Sciences, University of Cambridge, Downing Street, Cambridge, CB2 3EQ, UK
[c] Neutron Program for Materials Research, Chalk River Laboratories, Chalk River, Ontario, Canada K0J 1J0

ARTICLE INFO

Article history:
Received 31 August 2008
Received in revised form
12 November 2008
Accepted 13 November 2008
Available online 21 November 2008

Keywords:
Pyrochlore
Fluorite
Ordered defect fluorite

ABSTRACT

The crystal structures of the compounds $La_{2-x}Y_xZr_2O_7$ and $La_{2-x}Y_xHf_2O_7$ with $x = 0.0$, 0.4, 0.8, 1.2, 1.6, and 2.0 have been studied using neutron powder diffraction and electron microscopy to determine the stability fields of the pyrochlore and fluorite solid solutions. The limits of pyrochlore stability in these solid solutions are found to be close to $La_{0.8}Y_{1.2}Zr_2O_7$ and $La_{0.4}Y_{1.6}Hf_2O_7$, respectively. In both systems the unit cell parameter is found to vary linearly with Y content across those compositions where the pyrochlore phase is stable, as does the x-coordinate of the oxygen atoms on the 48f ($x,\frac{3}{8},\frac{3}{8}$) sites. In both systems, linear extrapolations of the pyrochlore data suggest that the disordering is accompanied by a small decrease in the lattice parameter of approximately 0.4%. After the pyrochlore solid solution limit is reached, a sharp change is observed from $x\sim0.41$ to 0.375 as the disordered defect fluorite structure is favoured. Electron diffraction patterns illustrate that some short-range order remains in the disordered defect fluorite phases.

© 2008 Elsevier Inc. All rights reserved.

1. Introduction

The pyrochlore structure type has great many uses, examples of which include magnetic materials [1,2], oxide fast ion conductors [3–6], and matrices for immobilisation of highly active radionuclides from nuclear wastes [7–10]. The last two applications are currently of major interest, as in both cases pyrochlores are capable of overcoming many technological problems, whilst remaining cost effective. The ideal pyrochlore structure type [11,12], $A_2B_2X_6Z$, is a superstructure of the fluorite (MX_2) structure, and is based upon a $2\times2\times2$ super cell with Fd $\bar{3}m$ symmetry, while that of the parent fluorite is Fm$\bar{3}m$. A schematic of the crystal structure is shown in Fig. 1, along with a comparison of the fluorite equivalent.

The cation superstructure of pyrochlore is based upon ordering of A and B cations parallel to the ⟨110⟩ directions, separated by ($\frac{111}{222}$), with respect to the origin. Using Wyckoff notation, for origin choice 2 and placing A at the origin, these are located on the 16c (000) and 16d ($\frac{111}{222}$) atomic positions, respectively, both having 3 m site symmetry. The A cation adopts a distorted cubic coordination with oxygen, while B is octahedrally coordinated. There are three crystallographically distinct anion sites in the pyrochlore lattice, two of these are the occupied X and Z sites on 48f ($x\frac{11}{88}$) and 8a ($\frac{111}{888}$), respectively. The third site is on 8b ($\frac{333}{888}$) and is normally vacant. This 48f site has site symmetry of 2mm, whereas 8a and 8b have site symmetry of $\bar{4}3m$. The vacancy on 8b allows the adjacent O^{2-} anions on 48f to relax and change position from $x = 0.375$ in the ideal fluorite structure to $x\sim0.419$ in the example of $La_2Zr_2O_7$.

Ordered pyrochlore is favoured when the radius ratio (r_A/r_B) [13] of the cations lies within the range 1.46–1.78 (e.g., $La_2Zr_2O_7$, $r_A/r_B = 1.61$). However, if the radius ratio is higher than 1.78, then a monoclinic layered perovskite type structure is often formed (e.g., $La_2Ti_2O_7$, $r_A/r_B = 1.92$) [14]. Conversely, when the ratio is less than 1.46, a defect fluorite structure is favoured (e.g., $Y_2Zr_2O_7$, $r_A/r_B = 1.42$). In certain nominal pyrochlore solid solutions involving a significant decrease in r_A/r_B, an increase in cation disorder is observed and accompanied by anion disorder as the vacant 8b site becomes progressively occupied by partial removal of oxygen from the 48f and 8a sites. With increasing disorder, the x-coordinate of the 48f site changes towards the fluorite position, 0.375. Coupled with the observation that the total O^{2-} content remains constant, it is possible to describe fluorite using the pyrochlore structure, but with $\frac{7}{8}$ occupancy across all three O^{2-} sites.

The use of a pyrochlore to immobilise actinide elements has long been studied and compositions have been postulated as 'ideal'. However, the recoil from alpha-decay places strain on the

* Corresponding author at: Institute of Materials Engineering, Australian Nuclear Science and Technology Organisation, PMB 1, Menai, NSW 2234, Australia.
E-mail address: karl.whittle@ansto.gov.au (K.R. Whittle).

0022-4596/$ - see front matter © 2008 Elsevier Inc. All rights reserved.
doi:10.1016/j.jssc.2008.11.008

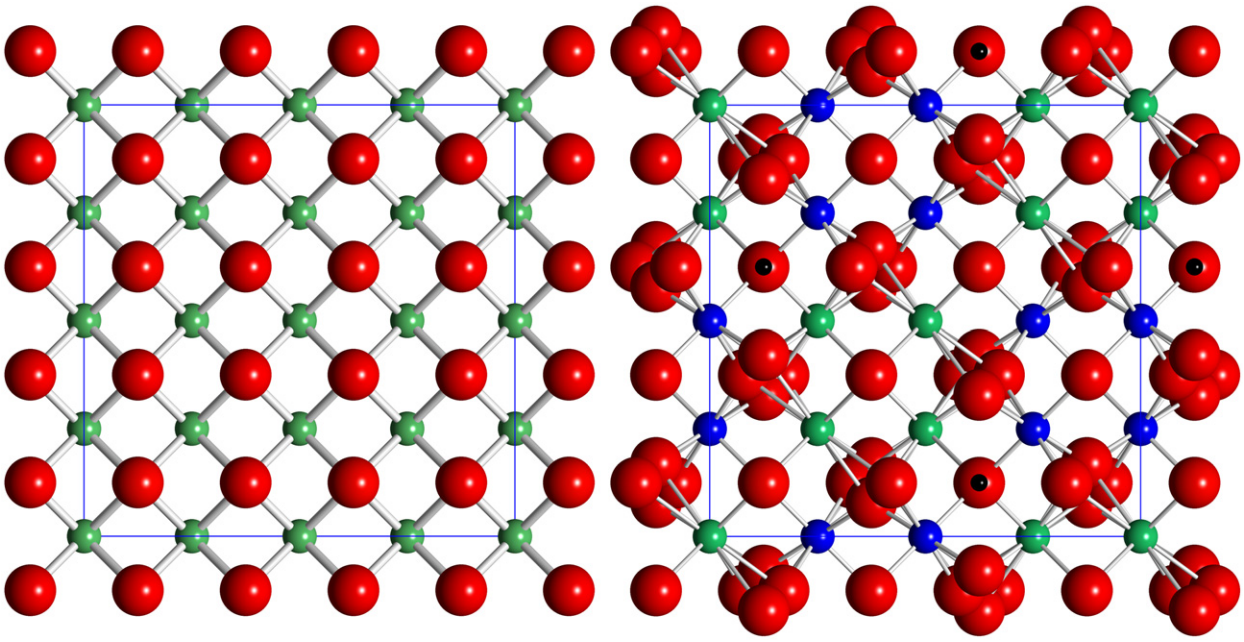

Fig. 1. Images of the crystal structures of fluorite (left) and pyrochlore (right). Projected along the [100] direction. The large red spheres are oxygen, the green (La/Y) and blue (Zr/Hf) smaller spheres are the cations. Small black spheres indicate the unoccupied 8*b* position. The fluorite cell has been generated using the pyrochlore structure with $x = 0.375$ hence the appearance of a larger unit cell.

lattice, which in some compositions causes the structure to become amorphous, while others are radiation tolerant [15–18]. The objective of this work is to study systematic yttrium addition on the $La_2Hf_2O_7$, and $La_2Zr_2O_7$ systems. As most trivalent actinide elements proposed as being immobilised in pyrochlore structures give rise to a cationic radius (r_A/r_B) ratio less than 1.48, it is important to examine the effect of such fluorite drivers on the stability of pyrochlore. Since Y^{3+} gives rise to a ratio less than 1.48, the results for this work will aid both simulations and ion-beam work [19] on similar systems.

2. Experimental procedures

2.1. Sample preparation

Samples based on $La_{2-x}Y_xZr_2O_7$ and $La_{2-x}Y_xHf_2O_7$ with $x = 0.4$, 0.8, 1.2, 1.6, and 2.0 were prepared by the calcination of metal oxides. Stoichiometric amounts of La_2O_3 (Aldrich, 99.5%), Y_2O_3 (Aldrich, 99%), ZrO_2 (Aldrich, 99.5%) and HfO_2 (Alfa-Aesar, 99%) were used. The powders were pre-fired at 850 °C and then intimately mixed in acetone using a ball-mill and dried. Once dried the powders were heated as pellets at 1500 °C for 7 days, reground to a fine powder, sufficient to pass through a 38 μm sieve, and reformed into pellets prior to a further heating at 1600 °C for 7 days. Portions of these sintered samples were ground to a fine powder, again sufficient to pass through a 38 μm sieve and used for diffraction analysis.

2.2. Electron microscopy and microanalysis

Samples were checked for purity by scanning electron microscopy and microanalysis (SEM–EDX) using a JEOL 6400 operating at 15 kV. Microanalyses were obtained using a Noran Voyager energy dispersive spectrometer attached to this microscope. The instrument was operated in standardless mode; however, the sensitivity factors were calibrated for semi-quantitative analysis using a range of synthetic and natural standard materials. Spectra were usually acquired for 500 seconds and reduced to weight percent oxides using a digital top hat filter to suppress the background, a library of reference spectra for multiple least squares peak fitting and full matrix corrections.

Selected samples were additionally analysed using transmission electron microscopy and microanalysis (TEM–EDX). TEM samples were prepared by crushing small fragments in methanol and collecting the suspension on holey carbon coated copper grids. Samples were using a JEOL 2000FXII TEM operated at 200 kV and calibrated for selected area diffraction over a range of objective lens currents using a gold film standard. The compositions of the grains were checked by EDX analysis using a Link ISIS energy dispersive spectrometer attached to the TEM. The *k*-factors required for the quantitative thin film analyses were determined from a range of synthetic and natural standard materials. Spectra were usually acquired for 600 seconds and processed using a digital top hat filter to suppress the background, a library of reference spectra for multiple least squares peak fitting, and a Cliff–Lorimer ratio procedure to reduce the data to weight percent oxides (details are given in Lumpkin et al. [20]).

2.3. Neutron diffraction

Neutron diffraction was used to obtain information on both cations and anion locations in these materials as is more accurate in the determination of oxygen parameters in the presence of heavier metal atoms than X-ray diffraction. Constant wavelength neutron diffraction patterns were collected, from densely packed powder in thin-walled cylindrical vanadium cans, using the C2-DualSpec diffractometer at the Chalk River National Laboratory, Canada, operating at an incident wavelength of 1.3283 Å (determined using an Al_2O_3 standard). Diffraction patterns were collected over the angular range 5°–120° 2θ, with an angular resolution of 0.1°, corresponding to a *d*-spacing range of 0.767–15.226 Å, and at a temperature of 298 K. The set of instrumental and structural parameters refined were an overall

scale factor, lattice parameters, a background function (Chebyschev polynomial), the widths of the Gaussian and Lorentzian components of the reflection line shape function, the *x*-coordinate of the O(1) atom on the 48*f* site, and isotropic displacement parameters for each site. Absorption correction parameters for cylindrical samples were calculated from the masses and volumes of samples loaded and not refined. The attenuation corrections applied were those calculated using standard practices. Structure refinement was by the Rietveld method [21] using the GSAS [22] suite of software with the additional EXPGUI toolkit [23]. The fit index values for determining the quality of fit were R_p and wR_p [22]. The compositions used in the Rietveld refinement of each phase were based on those from the electron microanalysis, with the overall scale of each phase being refined.

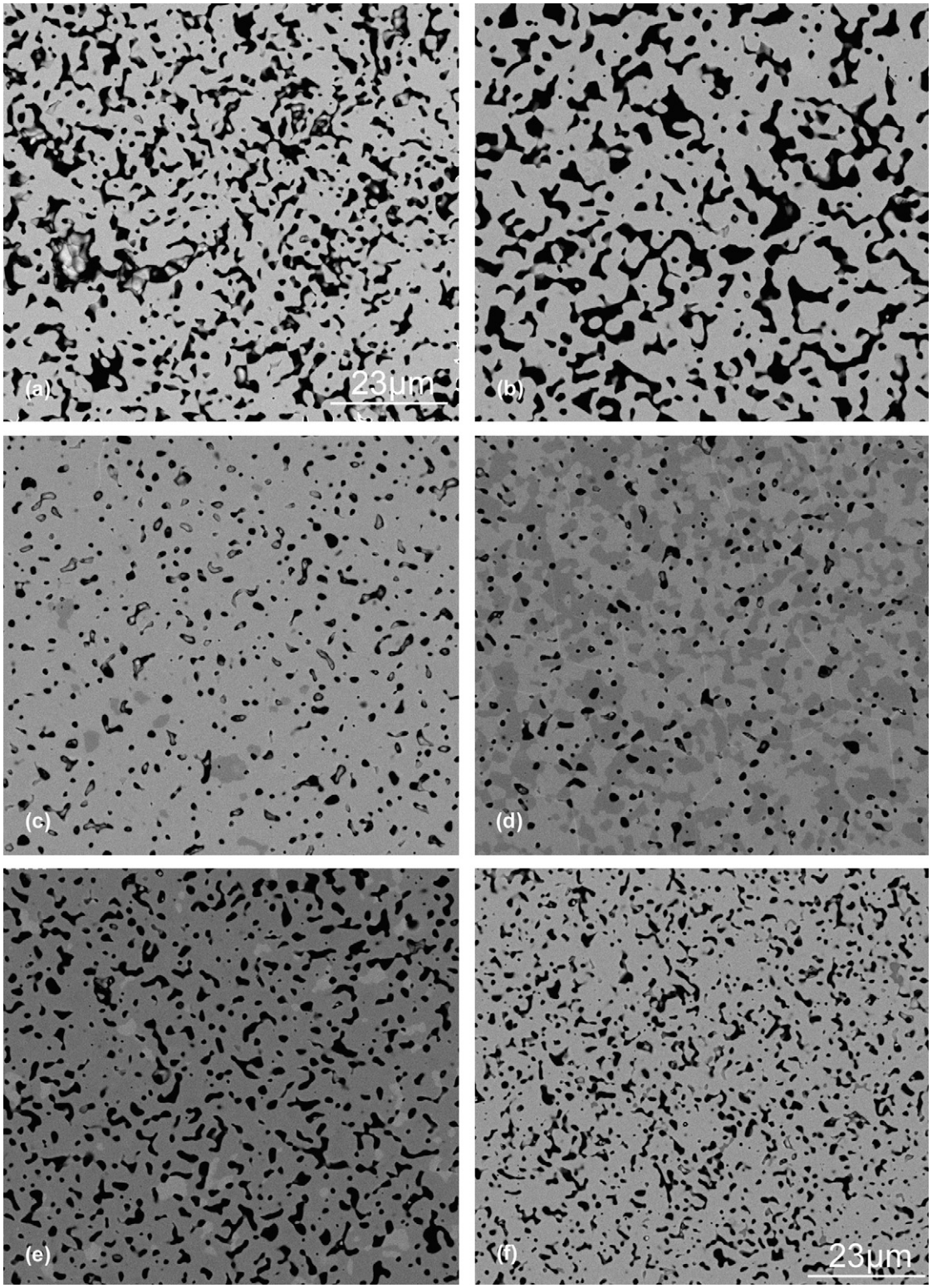

Fig. 2. Backscattered electron (BSE) images from $La_{2-x}Y_xZr_2O_7$ showing the various phases in each sample. The sub-images are: (a) $x = 0.0$, (b) $x = 0.4$, (c) $x = 0.8$, (d) $x = 1.2$, (e) $x = 1.6$, and (f) $x = 2.0$. As can be seen in (d) the mixture seems to be two phase, while (c) and (e) are two phase with a smaller amount of the secondary phase.

3. Results

3.1. Microstructure and chemistry

SEM observations revealed that the materials are reasonably sintered given the refractory nature of the compositions. Back-scattered electron images (see Fig. 2) of samples in the $La_{2-x}Y_xZr_2O_7$ series reveal that the products are single phase up to the nominal composition with $x = 0.8$ Y atoms per formula unit; however, this sample only contains 1–2% of the defect fluorite phase. The sample with nominal $x = 1.2$ contains roughly equal proportions of pyrochlore and defect fluorite. We also observed about 1–2% of the pyrochlore phase in the sample with $x = 1.6$, suggesting that the limit of defect fluorite solubility is

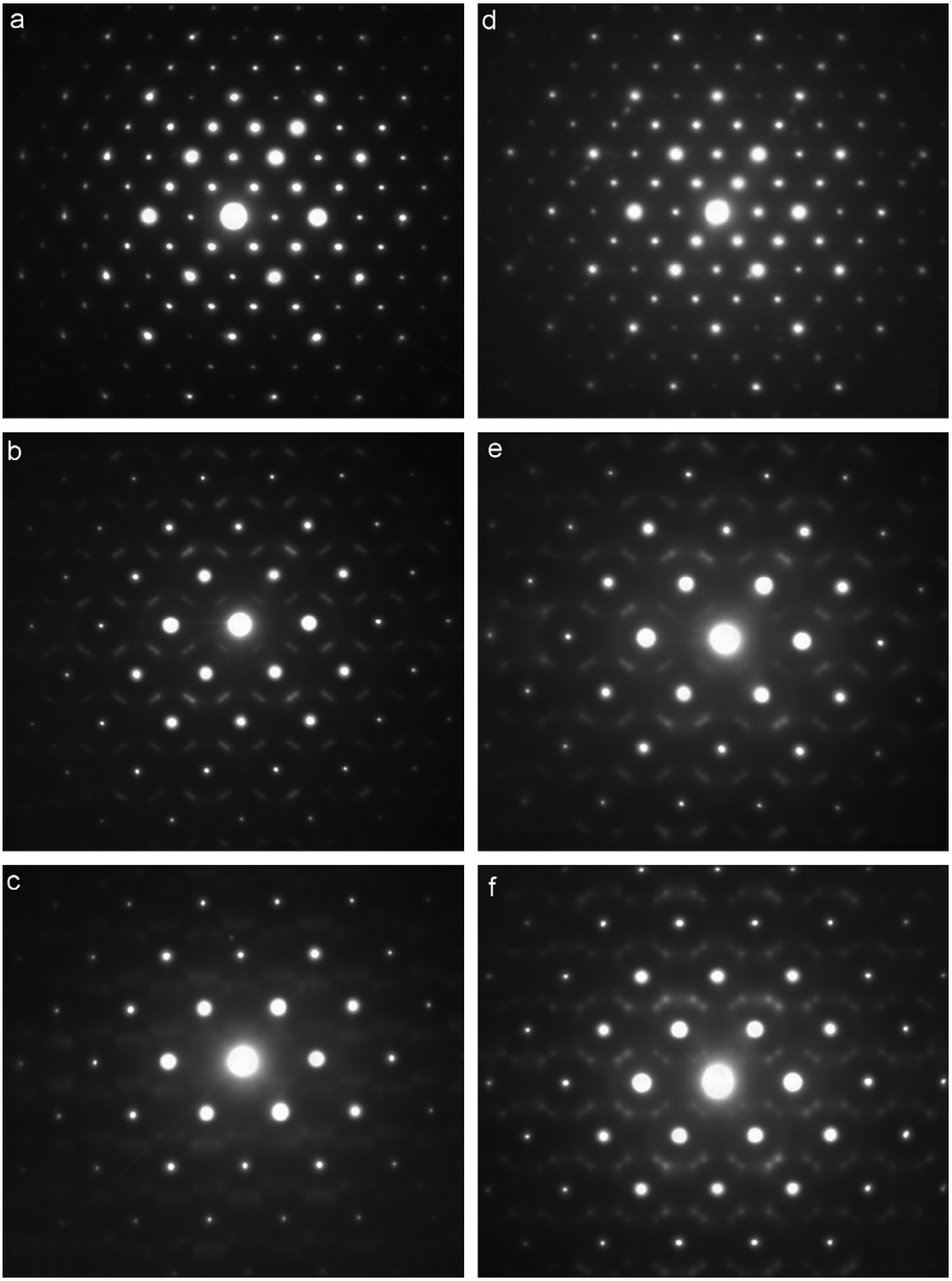

Fig. 3. Selected area electro diffraction images of (a) $La_{0.8}Y_{1.2}Zr_2O_7$, (b) $La_{0.4}Y_{1.6}Zr_2O_7$, (c) $Y_2Zr_2O_7$, (d) $La_{0.4}Y_{1.6}Hf_2O_7$ (pyrochlore phase), (e) $La_{0.4}Y_{1.6}Hf_2O_7$ (fluorite phase), and (f) $Y_2Hf_2O_7$. The diffraction patterns are from the [110] zone axis. The sub images (b), (c), (e), and (f) show evidence for short range ordering in the fluorite phase.

close to $x \sim 1.61$ in this system. Due to the fine grain structure and limited resolution of our SEM, we did not observe the two-phase region in images of the $La_{2-x}Y_xHf_2O_7$ samples; however, electron diffraction work clearly shows the presence of a two-phase region in the sample with $x = 1.6$.

Elemental analysis by SEM–EDX analyses confirmed that all of the single-phase pyrochlore samples in both series and the two Y end-member defect fluorite samples are very close to the nominal compositions (generally within ± 0.02–0.03 atoms per formula unit). However, we encountered difficulty in obtaining good quality analyses in the two-phase region due to the small grain size and resulting X-ray generation from surrounding grains. In the $La_{0.8}Y_{1.2}Zr_2O_7$ sample the estimated compositions of the coexisting pyrochlore and defect fluorite phases are approximately $x = 0.8$ and 1.7 Y atoms per formula unit, respectively. More reliable TEM–EDX analyses give compositions of $x = 0.9$ for the pyrochlore phase and $x = 1.6$ for the defect fluorite phase in this sample. No reliable SEM–EDX analyses were obtained in the two-phase region of the Hf samples due to the grain size, thus we rely solely on the TEM–EDX data which put the compositions of the coexisting pyrochlore and defect fluorite phases at close to $x = 1.5$ and 1.9, respectively, in the $La_{0.4}Y_{1.6}Hf_2O_7$ sample.

We also recorded the selected area diffraction (SAED) patterns of the pyrochlore and defect fluorite phases in both of the primary two-phase samples noted above and the two Y end-members. These were taken in the [110] zone axis orientation and representative patterns are illustrated in Fig. 3. In both samples, the pyrochlore phase exhibits the classical pattern of sharp and distinct pyrochlore superlattice diffraction intensities with somewhat stronger fluorite subcell intensities (Figs. 3a and d). We did not observe evidence for structured diffuse scattering of the cristobalite type, represented by $\{110\}^*$ sheets of diffuse intensity, as found by Tabira et al. [24] in quenched samples of $La_2Zr_2O_7$. In $La_{0.8}Y_{1.2}Zr_2O_7$, $La_{0.4}Y_{1.6}Hf_2O_7$, and $Y_2Hf_2O_7$, we observe strong diffracted intensity characteristic of the fluorite subcell and diffuse scattering that appears to be split into a pair of nodes lying on either side of the $G_F \pm \frac{1}{2}\langle 111 \rangle^*$ regions of reciprocal space (Figs. 3b, e, and f). These pairs of nodes are actually sections through rings of diffuse intensity oriented normal to the $\langle 111 \rangle^*$ directions [24–28]. The magnitude of the node splitting, and hence the ring diameter, is on the order of 0.04–0.07 $Å^{-1}$ normal to $\langle 111 \rangle^*$ and appears to increase from $La_{0.4}Y_{1.6}Hf_2O_7$ (0.040 ± 0.004 $Å^{-1}$) to $La_{0.4}Y_{1.6}Zr_2O_7$ (0.043 ± 0.001 $Å^{-1}$) to $Y_2Hf_2O_7$ (0.059 ± 0.001 $Å^{-1}$), observed intensities are shown in Fig. 4, with fits describing the peak positions. The magnitude of these splits corresponds to the inverse of the interaction distance, and is found to decrease from 23.3 ± 0.5 Å in $La_{0.4}Y_{1.6}Hf_2O_7$ to 16.9 ± 0.3 Å in $Y_2Hf_2O_7$. Such a decrease indicates the length of interaction is decreasing, but is still not commensurate with the measured fluorite unit cell, Table 1. The explanation for this is the subject of current work and will be the focus of a further publication.

The SAED patterns for the end-member $Y_2Zr_2O_7$ appear to have weaker diffuse scattering and the intensity distribution is

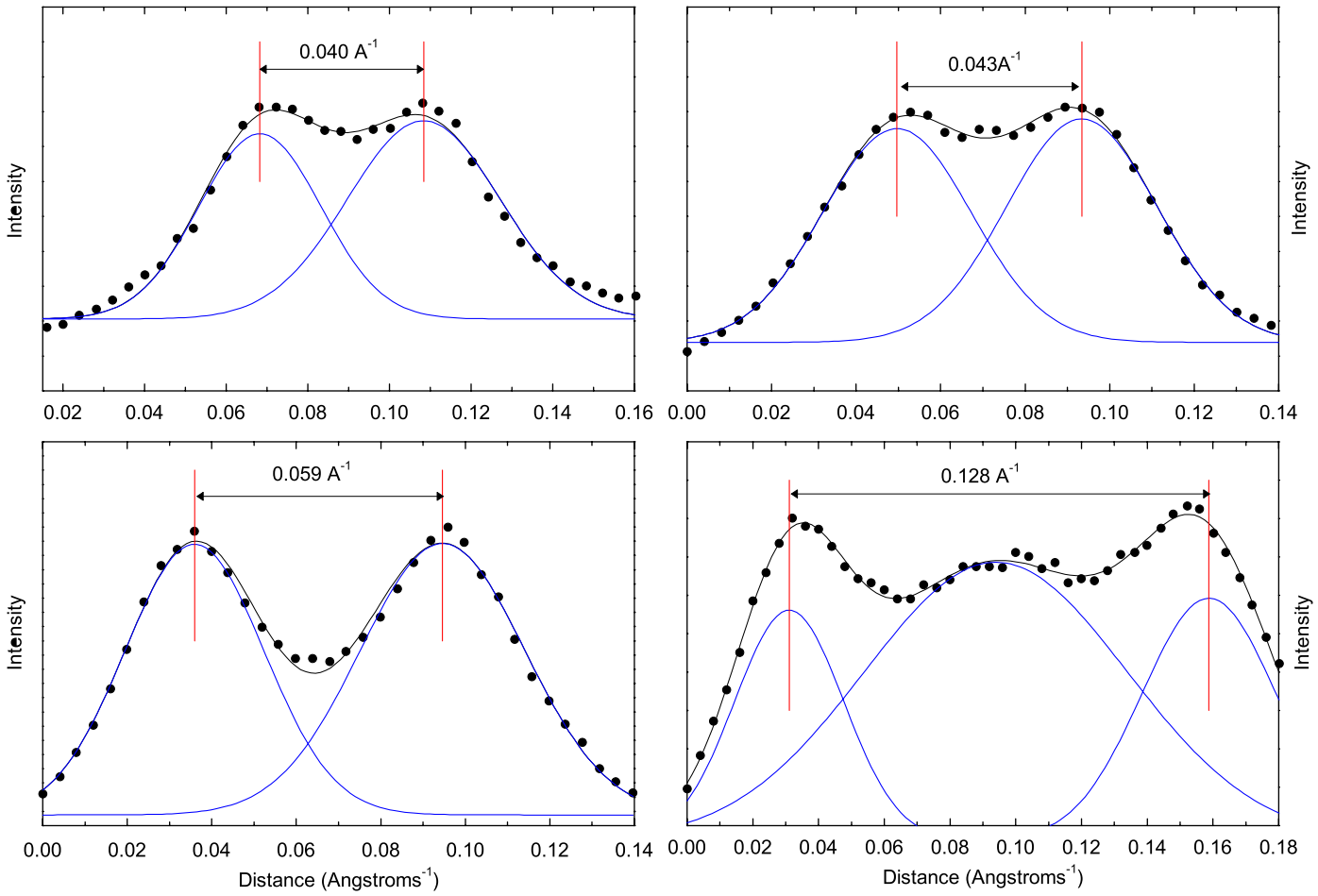

Fig. 4. Plots of intensity against distance^{-1} between the spots indicative of fluorite ordering. The sub plots are (a) $La_{0.4}Y_{1.6}Hf_2O_7$, (b) $Y_2Hf_2O_7$, (c) $La_{0.4}Y_{1.6}Zr_2O_7$, and (d) $Y_2Zr_2O_7$. $Y_2Zr_2O_7$ shows evidence of three intensities; the outer two spots are used in determination of the correlation length, with a subsequent geometrical correction to calculate the distance.

Table 1
Results obtained from the Rietveld refinements.

Ideal system	A (Å)	48*f*	Wt Frac	wR_p	R_p
$La_2Hf_2O_7$	10.7728(3)	0.4202(2)	1	0.0519	0.0387
$La_{1.6}Y_{0.4}Hf_2O_7$	10.7212(3)	0.4185(2)	1	0.0505	0.0383
$La_{1.2}Y_{0.8}Hf_2O_7$	10.6460(3)	0.4166(2)	1	0.0488	0.0358
$La_{0.8}Y_{1.2}Hf_2O_7$	10.5718(3)	0.4124(2)	0.98(1)	0.0492	0.0373
	5.1955(1)		0.02(1)		
$La_{0.4}Y_{1.6}Hf_2O_7$	10.5148(5)	0.4093(37)	0.57(1)	0.0518	0.0401
	5.2116(3)		0.43(1)		
$Y_2Hf_2O_7$	5.1958(2)		1	0.0696	0.0528
$La_2Zr_2O_7$	10.8076(5)	0.4189(2)	1	0.0732	0.044
$La_{1.6}Y_{0.4}Zr_2O_7$	10.7484(4)	0.4174(2)	1	0.0685	0.044
$La_{1.2}Y_{0.8}Zr_2O_7$	10.6714(4)	0.4140(2)	1	0.0674	0.0443
$La_{0.8}Y_{1.2}Zr_2O_7$	10.6572(5)	0.4134(3)	0.58(1)	0.0605	0.0428
	5.2428(3)		0.42(1)		
$La_{0.4}Y_{1.6}Zr_2O_7$	5.2469(2)		1	0.0548	0.0379
$Y_2Zr_2O_7$	5.2105(2)		1	0.0486	0.0332

The values shown are the unit cell size, *x* in 48*f*, phase fractions were appropiate and the wR_p and R_p values [22].The errors quoted are those presented by GSAS, and are shown as the error in the last digit. The systems where no 48*f*-*x* position is quoted are the observed fluorite phase.

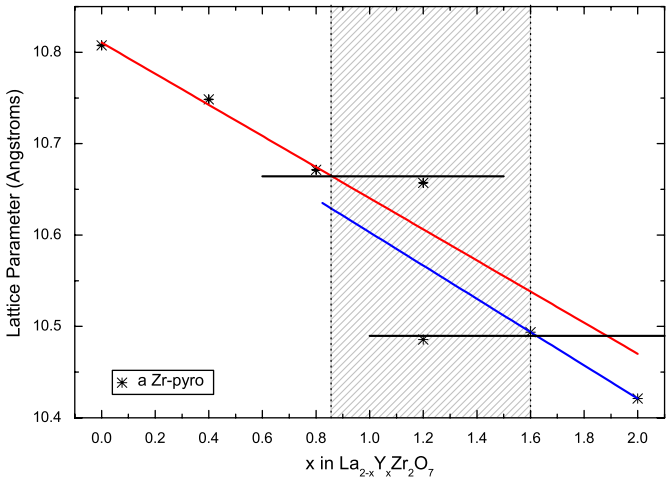

Fig. 5. Plot of lattice parameter against composition in $La_{2-x}Y_xZr_2O_7$. The values for the fluorite unit cell have been doubled to be consistent with the pyrochlore lattice. The linear fits to the points have been extended showing the estimated size based on pyrochlore and fluorite ordering. The hatched region indicates the expected two-phase region; see Harvey et al. [43].

different to that of the other samples (Fig. 3e). This material still shows the $G_f \pm \frac{1}{2}\langle 111\rangle^*$ type splitting in the [110] zone axis; however, the magnitude of the splitting of the nodes is greater and there exists a diffuse scattering distribution between the nodes oriented normal to the $\langle 110\rangle^*$ directions in reciprocal space. This scattering distribution appears to be due in part to a third node of the type $G_f \pm (\frac{1}{4}+x)\langle 220\rangle^*$ located between the other two nodes. The modulation features in this composition result in a pattern of diffuse triplets extending parallel to $\langle 001\rangle^*$ with a characteristic offset normal to the $\langle 110\rangle^*$ direction of the defect fluorite lattice. Analysis of these peaks gives a distance of 0.090 ± 0.001 Å^{-1}, which gives a correlation distance of 11.1 ± 0.2 Å, which is smaller than that observed for $La_{0.4}Y_{1.6}Zr_2O_7$. As a final observation, none of the defect fluorite SAEDs showed evidence for scattering at the $G_f \pm \langle 100\rangle^*$ regions of reciprocal space. Similar results have been seen with other defect fluorite systems, e.g. Y_2O_3–Nb_2O_5 [29].

3.2. Neutron diffraction

The results from the Rietveld refinements are shown in Table 1, where we report the lattice parameter, *x*-coordinate of the 48*f* position, the refined weight fractions of the coexisting pyrochlore and defect fluorite phases, and the crystallographic R_p and wR_p factors. In the $La_{2-x}Y_xZr_2O_7$ solid solution series we found the samples to be single-phase pyrochlore for $x = 0.0$–0.8. For the sample with $x = 1.2$, the refinements gave 58 wt% pyrochlore and 42 wt% defect fluorite. This distribution agrees with the relative proportions found by SEM analysis using back-scattered electrons, Fig. 2(d). No second phase was found in the sample with $x = 1.6$. There is a minor discrepancy between the diffraction and electron microscopy data for the samples with $x = 0.8$ and 1.6, where we found about 1–2% defect fluorite by SEM imaging. It is not unreasonable to have missed this small amount of second phase as it is within 2–3 standard deviations of the typical error in the Rietveld phase analysis procedure. The lattice parameters (doubled for the defect fluorite) are shown in Fig. 5 plotted against the nominal sample compositions. The diagonal lines show the trends in the single-phase fields, and are fitted using a linear equation. The pyrochlore line, extrapolated into the defect fluorite field, indicates that the lattice parameter is higher that the equivalent defect fluorite by about 0.04 Å. The horizontal lines, drawn through the points in the main two-phase field, indicate that the compositions of the coexisting pyrochlore and defect fluorite phases are approximately $La_{1.1}Y_{0.9}Zr_2O_7$ and $La_{0.36}Y_{1.64}Zr_2O_7$, respectively.

In the $La_{2-x}Y_xHf_2O_7$ series the samples with $x = 0.0$–0.8 were also found to be single-phase pyrochlore with no detectable secondary phase. The next sample in the series based on the composition $La_{0.8}Y_{1.2}Hf_2O_7$ was found by neutron diffraction to contain a small amount of the defect fluorite phase (~2%), but only showed the (111) reflection, just enough for determination of the unit cell parameter and an estimate of phase fraction. The ability of neutron diffraction to see such a small amount of phase is due, in this case, to both samples being cubic, but with a significant difference in lattice parameter for the peaks to be separated. This is not always the case, particularly where the phases are non-cubic and have overlapping peaks. For the sample with $x = 1.6$, the refinements gave 57 wt% pyrochlore and 43 wt% defect fluorite. This was the only composition that showed two phases in appreciable amounts. In both systems, the linear decrease in lattice parameter for the pyrochlore phase is found to agree with Vegard's law for cubic systems and is directly related to the change in average ionic radius from La^{3+}(1.16 Å) to Y^{3+} (1.019 Å). This agrees with previously published results based on lattice simulations of disordered pyrochlores [30–34].

The change in the value of the *x*-coordinate of the 48*f* position as a function of increasing Y content is more complex and is illustrated for both systems in Fig. 6. In both cases, excluding the data points in the principal two-phase regions, the variation of the *x*-coordinate of the pyrochlore phase appears to be non-linear with composition. This change is found to adopt a similar quadratic profile as reported by Heremans et al. [35] for the $Y_2Ti_{2-x}Zr_2O_7$ system. Both data points representing the pyrochlore phases in their respective two-phase regions can be interpreted in a similar fashion to the lattice parameters. Thus, the intersection of the horizontal lines with the curves shown in Fig. 6 gives the compositions of the pyrochlore phases. In this case, we find that the data provide estimates of $x = 0.86$ for the Zr sample and $x = 1.47$ for the Hf sample.

Using similar procedures for refinement previously suggested by Wuensch et al. [36], it is possible to obtain the degree of anionic disorder independently of cation disorder. This technique was only possible in those samples where the pyrochlore phase was dominant, in some cases the degree of overlap between the

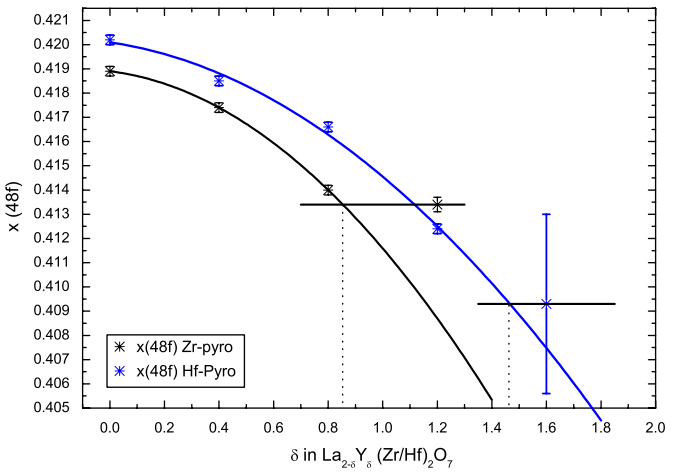

Fig. 6. Plots of 48*f*-*x* position against *x* in $La_{2-x}Y_xZr/Hf_2O_7$. The curves are quadratic fits to those positions that come from observable single phase refinements. The horizontal lines link the position from two-phase samples, and give an indication of the composition limit of these phases.

Table 2
The values obtained from anion site mixing.

Ideal system	Frac-48*f*	Frac-8*a*	Frac-8*b*
$La_2Hf_2O_7$	1	1	0
$La_{1.6}Y_{0.4}Hf_2O_7$	1	1	0
$La_{1.2}Y_{0.8}Hf_2O_7$	0.997(3)	0.983(18)	0.044(23)
$La_{0.8}Y_{1.2}Hf_2O_7$	0.980(3)	0.995(17)	0.168(24)
$La_{0.4}Y_{1.6}Hf_2O_7$	0.978(6)	0.945(34)	0.235(45)
$La_2Zr_2O_7$	1	1	0
$La_{1.6}Y_{0.4}Zr_2O_7$	0.994(2)	1	0.049(16)
$La_{1.2}Y_{0.8}Zr_2O_7$	0.981(2)	1	0.152(17)
$La_{0.8}Y_{1.2}Zr_2O_7$	0.979(2)	1	0.168(24)

The errors quoted are those presented by GSAS and are shown as the error in the last digit.

pyrochlore and fluorite phases prevented those peaks under refinement from being isolated sufficiently. In those samples where the diffraction data showed a single phase, the 'ideal' composition was used. The anionic disorder was found to start at $x = 0.4$ in the $La_{2-x}Y_xZr_2O_7$ series and at $x = 0.8$ in the $La_{2-x}Y_xHf_2O_7$ series. In both of the pyrochlore solid solutions we found the refined 8b site occupancy is nearly the same and reaches a level of ~0.15–0.17, representing approximately 15–20% disorder at the beginning of the two-phase regions. As expected the degree of disorder is directly linked to the observed *x*-coordinate of the 48*f* position, in that when disorder begins the oxygen atoms on the 48*f* sites start to relax towards an *x*-coordinate of 0.375, the value for the defect fluorite structure. The relaxation is greater in the Hf pyrochlores because the two-phase field begins at a much higher Y content (see Tables 1 and 2). As expected, the relationship between the *x* anion coordinate and the degree of disorder is effectively linear.

4. Comparison with predicted values

If both sets of samples are compared with the predicted values for unit-cell sizes, based on statistical analysis of published data, from Chakoumakos [11], Eq. (1) presented in Table 3 and Fig. 7, there is close agreement in samples which show pyrochlore as the predominant phase:

$$a = 1.914R_A + 2.91R_B + 6.422 \quad (1)$$

Table 3
Comparison of measured unit cell values and those predicted by Chakoumakos [11].

Ideal system	Measured	Predicted	Difference
$La_2Hf_2O_7$	10.7728(3)	10.6872(0.0133)	0.0855
$La_{1.6}Y_{0.4}Hf_2O_7$	10.7212(3)	10.6671(0.0609)	0.0541
$La_{1.2}Y_{0.8}Hf_2O_7$	10.6460(3)	10.6063(0.0477)	0.0397
$La_{0.8}Y_{1.2}Hf_2O_7$	10.5718(3)	10.5456(0.0774)	0.0261
$La_{0.4}Y_{1.6}Hf_2O_7$	10.5148(5)	10.4463(0.0420)	0.0685
$La_2Zr_2O_7$	10.8076(5)	10.7152(0.0333)	0.0924
$La_{1.6}Y_{0.4}Zr_2O_7$	10.7484(4)	10.7111(0.0306)	0.0373
$La_{1.2}Y_{0.8}Zr_2O_7$	10.6714(4)	10.6719(0.0306)	−0.0005
$La_{0.8}Y_{1.2}Zr_2O_7$	10.6572(5)	10.6335(0.0612)	0.0237

The errors in the predicted values are based on the compositional errors from the electron microanalysis and are shown as the absolute error; all the other errors are shown as those in the last digit.

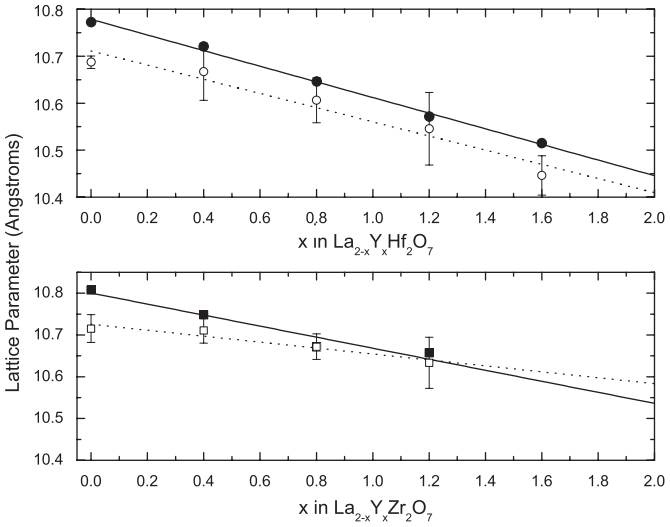

Fig. 7. Refined unit-cell sizes obtained using GSAS (solid circles and line) and predicted unit-cell sizes using the equation by Chakomouakos [11](empty circles and dotted line). (a) The values obtained for the $La_{2-x}Y_xHf_2O_7$ system and (b) for the $La_{2-x}Y_xZr_2O_7$ system.

However, once cationic/anionic disorder happens, the agreement is not so good. The deviation from Eq. (1) is primarily down to the assumptions used in the original generation and the ionic radii used. The ionic radius of an element is determined by both it's charge and coordination, for example Hf^{4+} has an ionic radius of 0.71 Å in six-fold coordination [37,38], while in eight-fold coordination it is 0.83 Å, thus with any cation disorder, the values should disagree. Even though Eq. (1) does not agree with the refined data once disorder begins, it is still a valid tool in the prediction of unit-cell sizes for $A_2B_2O_7$ pyrochlores. The equation allows model parameters to be used in the structural possibilities for actinide containing pyrochlores.

5. Bond valence analysis

Bond valence analysis is a method that is routinely used for predicting bond lengths in unknown structures. However, it also provides a semi-empirical check on measured structures, and has been applied to these samples. The results obtained from this analysis are reported in Table 4. The calculated values for the bond valence sums, S_{ij}, to the A and B sites indicate that the deformation from the ideal pyrochlore structure is consistent with the effect of Y on the structure, i.e., the structure becomes more fluorite-like as the Y content is increased. The values of S_{ij} tend to remain around

Table 4
Bond valence summations calculated for the pyrochlore phases studied.

Ideal system	R_{ij}–La/Y	S_{ij}–La/Y	R_{ij}–Zr/Hf	S_{ij}–Zr/Hf
$La_2Hf_2O_7$	2.644(1) 2.332(1)	2.974(6)	2.090(1)	3.826(7)
$La_{1.6}Y_{0.4}Hf_2O_7$	2.619(1) 2.321(1)	2.913(5)	2.087(1)	3.854(6)
$La_{1.2}Y_{0.8}Hf_2O_7$	2.586(1) 2.305(1)	2.865(6)	2.081(1)	3.933(8)
$La_{0.8}Y_{1.2}Hf_2O_7$	2.538(1) 2.289(1)	2.879(6)	2.086(1)	3.915(8)
$La_{0.4}Y_{1.6}Hf_2O_7$	2.502(3) 2.277(1)	2.776(12)	2.089(2)	3.923(18)
$La_2Zr_2O_7$	2.643(2) 2.340(1)	2.952(8)	2.102(1)	3.700(10)
$La_{1.6}Y_{0.4}Zr_2O_7$	2.617(2) 2.327(2)	2.890(7)	2.097(1)	3.824(10)
$La_{1.2}Y_{0.8}Zr_2O_7$	2.574(2) 2.310(1)	2.990(8)	2.098(1)	3.778(11)
$La_{0.8}Y_{1.2}Zr_2O_7$	2.565(2) 2.307(1)	2.954(12)	2.098(2)	3.778(16)

R_{ij} are the bond lengths in Angstroms and S_{ij} is the bond valence summation. The errors in the final digit are presented and are based on the calculated errors in bond lengths which have been derived from the Rietveld refinements.

3 and 4 for the A and B sites, respectively. These values are in agreement with those previously published on bond valence analysis of order/disorder in pyrochlores [39].

6. General discussion

The data indicate that two-phase regions in $La_{2-x}Y_xZr_2O_7$ and $La_{2-x}Y_xHf_2O_7$ exist for composition ranges of $x = 0.8$–1.6 and $x = 1.2$–1.6, respectively. In the Hf series, the single-phase pyrochlore stability field extends to a composition much larger in Y than would be expected when predicted using radius ratio rules for the cations. The composition at which a pyrochlore structure is unfavoured is $La_{0.42}Y_{1.58}Hf_2O_7$, giving a cation radius ratio of 1.48. In these samples predominantly single-phase pyrochlore forms up to $La_{0.6}Y_{1.4}Hf_2O_7$, which gives a formal radius ratio of 1.44, below the predicted limit. In this sample however the composition by electron microanalysis was found to be slightly deficient in cations. It is likely that this deficiency gives the false impression that these samples should be fluorite instead of pyrochlore. In reality it is at the limit of the stability range, as shown in the next composition being entirely fluorite, shown by neutron diffraction.

In the $La_{2-x}Y_xZr_2O_7$ system the last pyrochlore containing composition is $La_{1.2}Y_{0.8}Zr_2O_7$ giving a cation radius ratio of 1.48. The next composition $La_{0.4}Y_{1.6}Zr_2O_7$ gives a ratio of 1.45, since this system is fully occupied on the A-site it is clearly within the expected fluorite range and is found to be fluorite. The anion disorder is found to increase across both systems, and shows that disorder begins to increase as the Y content increases; this is to be expected as Y drives the system to become fluorite, with an average $\frac{7}{8}$ occupancy for all oxygen positions.

Comparison with other pyrochlores doped with fluorite drivers [40] shows a similar process, the only major difference is the method for doping. In these samples the A-cation was exchanged while in Heremans et al. [40] the B-cation was exchanged. Slight differences in the process of disorder are found and are probably due to the different sample heating profiles, i.e., the longer the heating the more ordered the sample is likely to be. In this work the samples were heated at 1500–1600 °C for a total of 14 days, whereas Heremans et al. [40] use the Pechini process with heating at 1100 and 1350 °C each for 2 days. These different heating regimes can probably account for the discrepancies between the two sets of results, not discounting of course the differences in composition.

The recent work of Ashbrook et al. [41] using ^{89}Y MAS NMR shows that in the series $Y_2Ti_{2-x}Sn_xO_7$ there is effectively random disorder across the B-site between the Sn and Ti, it is expected that this process occurs in these samples between the Y and La. However, it is impossible to determine this from a single neutron diffraction pattern alone.

The difference in pyrochlore stability between the Hf and Zr series is more difficult to interpret, in the majority of cases Hf is often expected to behave in the same manner as Zr. However, in these samples this is not the case. It may simply be that since the ionic radius [37,38] of Zr^{4+} (0.72 Å) is closer to that of Y^{3+} (0.9 Å) than Hf^{4+} (0.71 Å), this small difference is enough to decrease the stability of the pyrochlore phase.

An example of a change in stability of phase between Zr and Hf based pyrochlores are the radiation tolerance of $La_2Zr_2O_7$, and $La_2Hf_2O_7$ [42]. In these samples it was found there was a large difference in the measured critical temperature for amorphisation (T_c), the temperature above which the sample crystallises at a rate greater than the damage accumulation rate. $La_2Zr_2O_7$ was found to have a T_c of 339 ± 49 K, while $La_2Hf_2O_7$ was 563 ± 10 K, which implies that $La_2Zr_2O_7$ is more 'stable' than $La_2Hf_2O_7$. As both Zr and Hf are in the same group (group IVB) and should behave in a similar manner, this is not always the case and they can behave differently.

7. Conclusion

The addition of a fluorite driver such as Y^{3+} in place of La^{3+} in pyrochlores containing Zr or Hf on the B site ultimately removes the superstructure and the compositional limit for a single phase fluorite is $1.4 < x < 1.6$ in the $La_{2-x}Y_xZr_2O_7$ series and for $1.6 < x < 2.0$ in the $La_{2-x}Y_xHf_2O_7$ series. The main two-phase region in the Hf-based pyrochlores is shifted to a much higher level of Y^{3+} doping than in the Zr-based series, close to $x = 1.2$ in these slowly cooled samples. For the same level of Y doping, the Hf samples are also more pyrochlore-like with regard to the systematically larger x-coordinate of the 48*f* oxygen position. TEM investigations illustrate that the defect fluorite phase exhibits evidence of short-range correlations in both systems, with the modulated structure being somewhat more ordered (e.g., pyrochlore-like) in the Hf-based samples. These results suggest that as a waste form pyrochlore based materials are ideal for elements such as U^{4+} and Pu^{4+}, which are both fluorite drivers.

References

[1] S.L. Chamberlain, S.T. Hess, L.R. Corruccini, Physics Letters A 323 (2004) 310–314.
[2] N.P. Raju, M. Dion, M.J.P. Gingras, T.E. Mason, J.E. Greedan, Physical Review B 59 (1999) 14489–14498.
[3] N. Kim, C.P. Grey, Journal of Solid State Chemistry 175 (2003) 110–115.
[4] J. Lian, L.M. Wang, S.X. Wang, J. Chen, L.A. Boatner, R.C. Ewing, Physical Review Letters 8714 (2001), (145901).
[5] F.W. Poulsen, M. Glerup, P. Holtappels, Solid State Ionics 135 (2000) 595–602.
[6] P.J. Wilde, C.R.A. Catlow, Solid State Ionics 112 (1998) 185–195.
[7] S.X. Wang, B.D. Begg, L.M. Wang, R.C. Ewing, W.J. Weber, K.V.G. Kutty, Journal of Materials Research 14 (1999) 4470–4473.
[8] S.X. Wang, L.M. Wang, R.C. Ewing, K.V.G. Kutty, Nuclear Instruments & Methods in Physics Research Section B—Beam Interactions with Materials and Atoms 169 (2000) 135–140.
[9] W.J. Weber, R.C. Ewing, Scientific Basis for Nuclear Waste Management XXV, vol. 713, Materials Research Society, Warrendale, 2002, pp. 443–454.
[10] S.V. Yudintsev, Geology of Ore Deposits 45 (2003) 151–165.
[11] B.C. Chakoumakos, Journal of Solid State Chemistry 53 (1984) 120–129.
[12] M.A. Subramanian, G. Aravamudan, G.V.S. Rao, Progress in Solid State Chemistry 15 (1983) 55–143.

[13] B.D. Begg, N.J. Hess, D.E. McCready, S. Thevuthasan, W.J. Weber, Journal of Nuclear Materials 289 (2001) 188–193.
[14] H.W. Schmalle, T. Williams, A. Reller, A. Linden, J.G. Bednorz, Acta Crystallographica Section B—Structural Science 49 (1993) 235–244.
[15] J. Lian, J. Chen, L.M. Wang, R.C. Ewing, J.M. Farmer, L.A. Boatner, K.B. Helean, Physical Review B 68 (2003), (134107).
[16] A. Meldrum, L.A. Boatner, R.C. Ewing, Physical Review Letters 8802 (2002), (025503).
[17] S. Zhu, X.T. Zu, L.M. Wang, R.C. Ewing, Applied Physics Letters 80 (2002) 4327–4329.
[18] J. Lian, X.T. Zu, K.V.G. Kutty, J. Chen, L.M. Wang, R.C. Ewing, Physical Review B 66 (2002) 054108.
[19] G.R. Lumpkin, K.R. Whittle, S. Rios, K.L. Smith, N.J. Zaluzec, Journal of Physics: Condensed Matter 16 (2004) 8557–8570.
[20] G.R. Lumpkin, K.L. Smith, M.G. Blackford, R. Giere, C.T. Williams, Micron 25 (1994) 581–587.
[21] H.M. Rietveld, Journal of Applied Crystallography 2 (1969) 65–71.
[22] A.C. Larson, R.B. Von Dreele, General Structure Analysis System (GSAS), Los Alamos National Laboratory Report LAUR 86-748, 2000.
[23] B.H. Toby, Journal of Applied Crystallography 34 (2001) 210–213.
[24] Y. Tabira, R. Withers, J. Thompson, S. Schmid, Journal of Solid State Chemistry 142 (1999) 393–399.
[25] Y. Liu, R.L. Withers, L. Noren, Journal of Solid State Chemistry 177 (2004) 4404–4412.
[26] Y. Tabira, R.L. Withers, J.C. Barry, L. Elcoro, Journal of Solid State Chemistry 159 (2001) 121–129.
[27] S. Garcia-Martin, M.A. Alario-Franco, D.P. Fagg, J.T.S. Irvine, Journal of Materials Chemistry 15 (2005) 1903–1907.
[28] P. Garcia-Chain, R.M. Rojas, P. Herrero, J.R. Gunter, Journal of Solid State Chemistry 108 (1994) 236–242.
[29] R. Miida, F. Sato, M. Tanaka, H. Naito, H. Arashi, Journal of Applied Crystallography 30 (1997) 272–279.
[30] L. Minervini, R.W. Grimes, K.E. Sickafus, Journal of the American Ceramic Society 83 (2000) 1873–1878.
[31] Y. Tabira, R.L. Withers, L. Minervini, R.W. Grimes, Journal of Solid State Chemistry 153 (2000) 16–25.
[32] M. Pirzada, R.W. Grimes, L. Minervini, J.F. Maguire, K.E. Sickafus, Solid State Ionics 140 (2001) 201–208.
[33] C.R. Stanek, R.W. Grimes, Journal of the American Ceramic Society 85 (2002) 2139–2141.
[34] M.J.D. Rushton, R.W. Grimes, C.R. Stanek, S. Owens, Journal of Materials Research 19 (2004) 1603–1604.
[35] K.W. Eberman, B.J. Wuensch, J.D. Jorgensen, Solid State Ionics 148 (2002) 521–526.
[36] B.J. Wuensch, K.W. Eberman, C. Heremans, E.M. Ku, P. Onnerud, E.M.E. Yeo, S.M. Haile, J.K. Stalick, J.D. Jorgensen, Solid State Ionics 129 (2000) 111–133.
[37] R.D. Shannon, Acta Crystallographica Section A A32 (1976) 751–767.
[38] R.D. Shannon, C.T. Prewitt, Acta Crystallographica Section B—Structural Science B 25 (1969) 925–946.
[39] B.J. Wuensch, K.W. Eberman, in: P. Vincenzini, V. Buscaglia (Eds.), Oxygen-Ion Conductivity, Disorder and Bonding in Pyrochlore Fuel–Cell Materials as a Function of Composition, Mass and Charge Transport in Inorganic Materials II, 2003.
[40] C. Heremans, B.J. Wuensch, J.K. Stalick, E. Prince, Journal of Solid State Chemistry 117 (1995) 108–121.
[41] S.E. Ashbrook, K.R. Whittle, G.R. Lumpkin, I. Farnan, Journal of Physical Chemistry B 110 (2006) 10358–10364.
[42] G.R. Lumpkin, K.R. Whittle, S. Rios, K.L. Smith, N.J. Zaluzec, Journal of Physics: Condensed Matter 16 (2004) 8557–8570.
[43] E.J. Harvey, K.R. Whittle, G.R. Lumpkin, R.I. Smith, S.A.T. Redfern, Journal of Solid State Chemistry 178 (2005) 800–810.